Field-free deterministic ultrafast creation of magnetic skyrmions by spin–orbit torques

Felix Büttner, Ivan Lemesh, Michael Schneider, Bastian Pfau, Christian M. Günther, Piet Hessing, Jan Geilhufe, Lucas Caretta, Dieter Engel, Benjamin Krüger, Jens Viefhaus, Stefan Eisebitt, Geoffrey S. D. Beach

Angaben zur Veröffentlichung / Publication details:

Büttner, Felix, Ivan Lemesh, Michael Schneider, Bastian Pfau, Christian M. Günther, Piet Hessing, Jan Geilhufe, et al. 2017. "Field-free deterministic ultrafast creation of magnetic skyrmions by spin–orbit torques." *Nature Nanotechnology* 12 (11): 1040–44. https://doi.org/10.1038/nnano.2017.178.

Field-free deterministic ultrafast creation of magnetic skyrmions by spin–orbit torques

Felix Büttner[1*†], Ivan Lemesh[1†], Michael Schneider[2], Bastian Pfau[2], Christian M. Günther[2,3], Piet Hessing[2], Jan Geilhufe[2], Lucas Caretta[1], Dieter Engel[2], Benjamin Krüger[4], Jens Viefhaus[5], Stefan Eisebitt[2,3] and Geoffrey S. D. Beach[1]

Magnetic skyrmions are stabilized by a combination of external magnetic fields, stray field energies, higher-order exchange interactions and the Dzyaloshinskii–Moriya interaction (DMI)[1–6]. The last favours homochiral skyrmions, whose motion is driven by spin–orbit torques and is deterministic, which makes systems with a large DMI relevant for applications. Asymmetric multilayers of non-magnetic heavy metals with strong spin–orbit interactions and transition-metal ferromagnetic layers provide a large and tunable DMI[4–8]. Also, the non-magnetic heavy metal layer can inject a vertical spin current with transverse spin polarization into the ferromagnetic layer via the spin Hall effect[9]. This leads to torques[10] that can be used to switch the magnetization completely in out-of-plane magnetized ferromagnetic elements, but the switching is deterministic only in the presence of a symmetry-breaking in-plane field[11–13]. Although spin–orbit torques led to domain nucleation in continuous films[14] and to stochastic nucleation of skyrmions in magnetic tracks[15], no practical means to create individual skyrmions controllably in an integrated device design at a selected position has been reported yet. Here we demonstrate that sub-nanosecond spin–orbit torque pulses can generate single skyrmions at custom-defined positions in a magnetic racetrack deterministically using the same current path as used for the shifting operation. The effect of the DMI implies that no external in-plane magnetic fields are needed for this aim. This implementation exploits a defect, such as a constriction in the magnetic track, that can serve as a skyrmion generator. The concept is applicable to any track geometry, including three-dimensional designs[16].

Magnetic skyrmions are particle-like spin textures in out-of-plane magnetized films, and are envisioned as information carriers to be created, deleted and shifted by currents in racetrack devices[17–19]. Their defining property is a spherical topology, which can be envisioned as a defect-free domain wall[1,20] that surrounds a central out-of-plane magnetized region whose size can be as small as a single point. Various concepts to create skyrmions have been proposed and demonstrated[4,6,15,21–27]. The concept of spin–orbit torque-induced nucleation is illustrated in the micromagnetic simulations in Fig. 1, using the example of a pinning site (area of reduced anisotropy) in a magnetic nanotrack. The down-magnetized (magnetization $m_z < 0$) track is exposed to $\mathbf{p} = -\hat{y}$ polarized magnetic moments that arise from the spin Hall effect of a charge current pulse along $+\hat{x}$, which generates damping-like and field-like spin–orbit torques (Methods). Complete switching of a ferromagnet by spin–orbit torques requires an external longitudinal field[11–13] (Supplementary Information). Here we observe local switching even without any in-plane fields applied, which becomes possible by combining the DMI with a non-uniform out-of-plane magnetization. Owing to the reduced anisotropy, the spin–orbit torque-induced reduction of $|m_z|$ is largest inside the defect (Fig. 1i), and thereby generates a gradient ∇m_z. The interfacial DMI that prefers left-handed domain walls (negative D_i) transforms this gradient into a field $\mathbf{H}_{\mathrm{DMI}} = (-2D_i)/M_s(\partial_x m_z, \partial_y m_z, -\partial_x m_x - \partial_y m_y)$ that points towards the defect (M_s, saturation magnetization). At the bottom-right side of the defect, $H_{\mathrm{DMI},y} > 0$ compensates the field-like spin–orbit torque and the longitudinal field $H_{\mathrm{DMI},x} < 0$ leads to switching of m_z. Once a reversed domain has formed, the moments in the domain wall align with the injected moments $\mathbf{p}$ wherever possible because of the field-like spin–orbit torque (Fig. 1j). The new bubble domain in Fig. 1j is topologically still equivalent to the uniformly magnetized state, that is, it has a topological charge of zero. This can be seen without calculation because, for a spin texture to be a skyrmion (that is, to have unit topological charge), all spin orientations must be present[2] and in Fig. 1j, $+y$ oriented moments are missing. The topological transition to a skyrmion happens at a later point.

In the simulations, we use a strong and short pulse to nucleate a reverse domain (write pulse) and a longer but weaker pulse to drive it away from the defect (shift pulse) (Fig. 1h). As illustrated in Fig. 1j–n, the weak pulse allows the magnetization in the domain wall to relax to the preferred left-handed (inward-pointing) chirality almost everywhere apart from a localized pair of vertical Bloch lines, which give the bubble domain a topological charge of zero. Subsequently, the left-handed Néel domain wall moves with the current and the Bloch lines remain nearly fixed in position. The centre of the domain thereby moves significantly away from the pinning centre. Once the current is switched off, the energetically unfavourable Bloch lines annihilate and the domain transforms into a topological skyrmion (Fig. 1n), which is similar to the behaviour of skyrmions nucleated by local spin injection[21]. In Figure 1b–h we demonstrate that an evenly spaced skyrmion bit sequence can be obtained by repeatedly injecting write-shift or shift-only current pulses, none of which ever reverses the skyrmions back to non-topological domains. Skyrmion trajectories have a negative y component because of the skyrmion Hall effect (Fig. 1f)[7,8]. Therefore, a 20 ns pause was included after each shift pulse to allow the skyrmions to return to the centre of the wire.

We now verify the predictions of the simulations experimentally using X-ray holography[2,28,29] with 15 repeats of Pt(2.7 nm)/$Co_{60}Fe_{20}B_{20}$(0.8 nm)/MgO(1.5 nm). Such multilayers have

[1]Department of Materials Science and Engineering, Massachusetts Institute of Technology, Cambridge, Massachusetts 02139, USA. [2]Max-Born-Institut, Max-Born-Straße 2A, 12489 Berlin, Germany. [3]Institut für Optik und Atomare Physik, Technische Universität Berlin, Hardenbergstraße 36, 10623 Berlin, Germany. [4]Institut für Lasertechnologien in der Medizin und Messtechnik an der Universität Ulm, Helmholtzstraße 12, 89081 Ulm, Germany. [5]Deutsches Elektronen-Synchrotron (DESY), FS-PE, Notkestraße 85, 22607 Hamburg, Germany. †These authors contributed equally to this work. *e-mail: felixbuettner@gmail.com

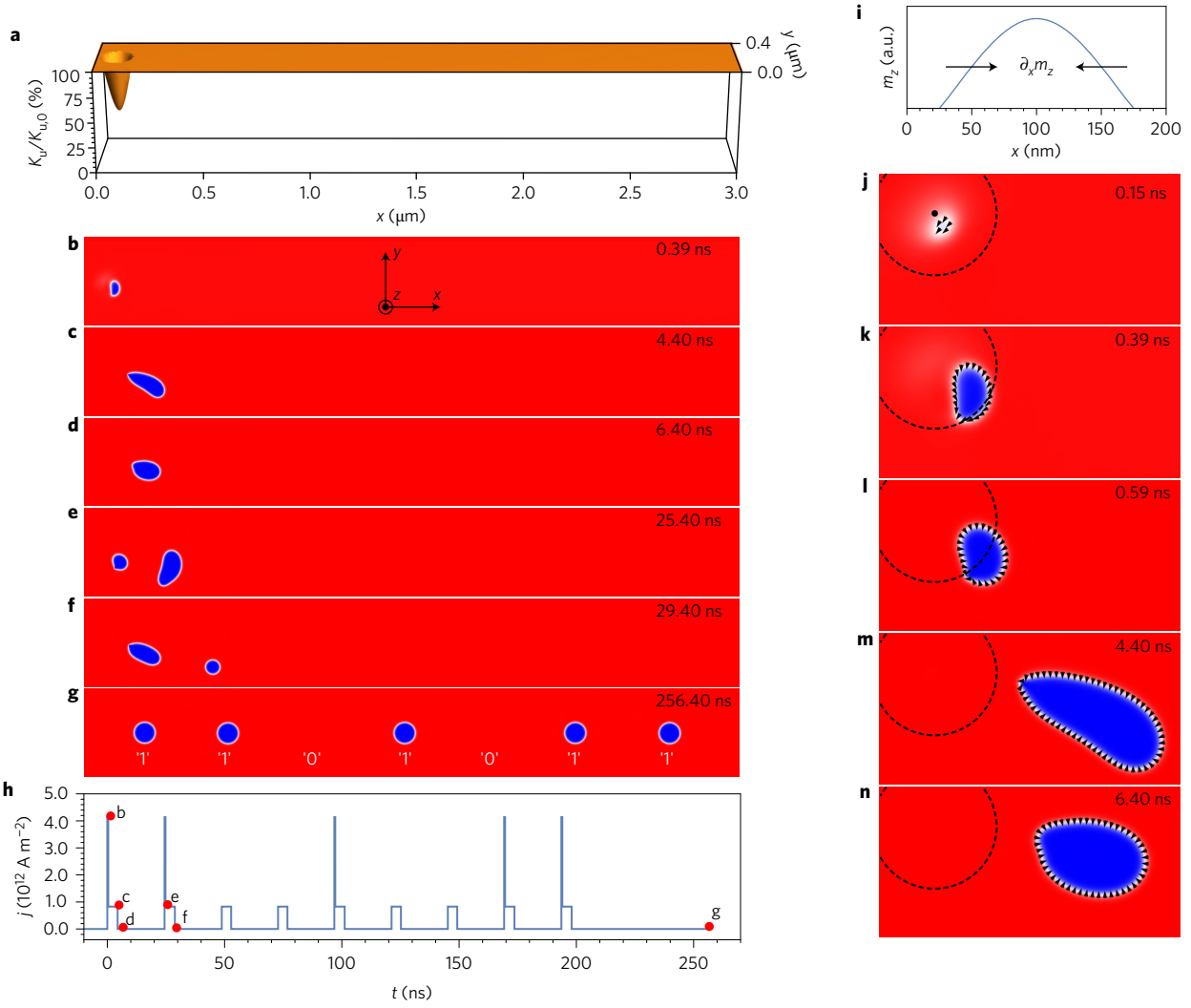

Figure 1 | Simulation of a bit sequence in a racetrack memory created by spin–orbit torque skyrmion generation near a pinning centre. a, Anisotropy distribution in the $3 \times 0.4\ \mu m^{-2}$ magnetic strip. The area of reduced anisotropy has a diameter of 150 nm and constitutes a pinning site, as typically found in sputtered multilayers. **b**–**g**, Temporal evolution of the magnetization in the strip after the injection of spin–orbit torque pulses (blue, $m_z > 0$; red, $m_z < 0$). **h**, The injected pulse pattern, also indicating the time corresponding to the snapshots **b**–**g**. The width of the write pulses is 0.4 ns, the width of the shift pulses is 4 ns and the relaxation in between lasts for 20 ns. Large pulse amplitudes are required because of a conservatively chosen value for the Gilbert damping of $\alpha = 0.5$ and the absence of temperature effects. The final skyrmion pattern in **g** corresponds to the bit sequence '1101011', with the presence (absence) of a skyrmion representing a logical '1' ('0') as depicted. **i**, Schematic cross-section of m_z across the defect at the start of the spin–orbit torque pulse (before the domain nucleation). The arrows indicate the sign of the gradient of m_z, pointing towards the centre of the defect. **j**–**n**, Magnification of the defect area. The defect circumference is sketched in each image by a dashed circle. The centre is marked with a black dot in **j**. The times in the images correspond to the pulse shape in **h**.

previously been shown to host left-handed Néel skyrmions because of the large DMI at the Pt/CoFeB interface[6,7]. The Pt also serves as a spin–orbit torque source. The film was patterned into a contacted track (Fig. 2a,b) aligned to a holographic field of view (FOV) for the imaging of m_z (Methods and Eisebitt *et al.*[28] and Büttner[29]). The magnetic state was imaged after a sequence of (1) saturating the film with a large z-axis bias field, (2) reducing the field to a value at which domains can exist but do not nucleate spontaneously and (3) injecting single rectangular-shaped spin–orbit torque current pulses or unipolar pulse trains. In Fig. 2c, we show the effect of injecting millions of current pulses before taking the image. Below a threshold current density of approximately $6.5 \times 10^{11}\,A\,m^{-2}$, stripe domains appear and the stripes are consistently oriented parallel to the injected current. In applications, these low current densities should hence be avoided. Above the threshold, skyrmions prevail. The images were recorded in the remanent field of the magnet ($\mu_0 H_z = -3.2$ mT as determined by reproducing exactly the same field history after the measurements). However, first, the field direction opposes the nucleated domains and skyrmions. Therefore, the out-of-plane field, if anything, inhibits the nucleation of reverse domains and cannot stabilize skyrmions against collapse. Second, the field is not responsible for stabilizing skyrmions from expanding into stripes in this material, because we observe stripe domains and skyrmions in the same applied field. Hence, skyrmions in this material are stabilized by pinning and the nucleation process does not require any external field to be applied.

The effect of single spin–orbit torque pulses is studied systematically in Fig. 3 as a function of pulse width τ and amplitude j. Reversed domains are generated with certainty for amplitudes above a sharp threshold $j_c(\tau)$. Figure 3a–f shows a selection of skyrmions generated by $\tau = 12$ ns and $j = 2.6 \times 10^{11}\,A\,m^{-2}$ pulses in a field of $\mu_0 H_z = -6.1$ mT. We find skyrmions in all images. The

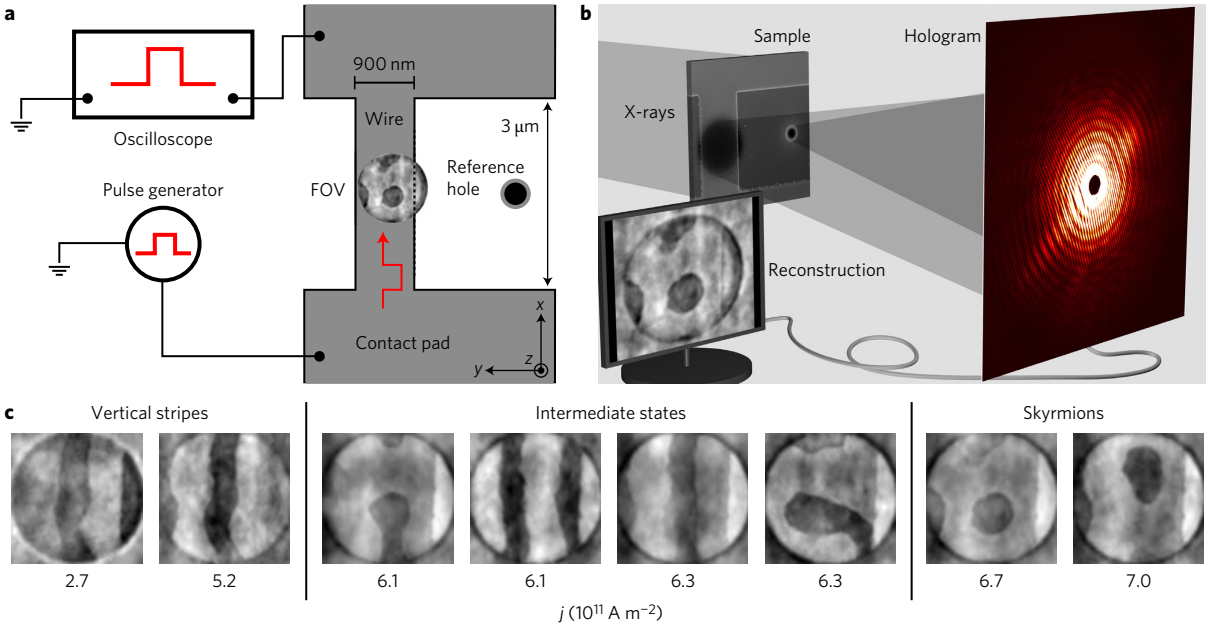

Figure 2 | Experimental set-up and the effect of pulse trains. a, Schematic overhead view of the sample and connection to the pulse electronics. The sample consists of an H-shaped magnetic material, the central part of which is the magnetic wire. The wire is 3 μm long and 900 nm wide. The centre of the wire is imaged holographically (see **b**) with a circular FOV. An example magnetic texture in the FOV is overlaid. Part of the FOV is outside of the wire, which makes it easy to recognize the image orientation. The wider parts of the magnetic material are connected to gold contact pads and from there to a pulse generator and an oscilloscope. **b**, Imaging set-up. The magnetic wire was grown on a transparent Si_3N_4 membrane. On the back side of the membrane, two holes were prepared in an opaque gold film. The larger one (1 μm in diameter) is aligned to the wire and defines the FOV. The second hole is point-like (with a diameter of typically a few tens of nanometres) and has a distance of 3 μm to the larger hole. It defines the reference beam for the holographic imaging. The structure is exposed to circularly polarized X-rays. The interference of the transmitted beam of the two holes forms the hologram, from which an image of the out-of-plane magnetization in the wire can be reconstructed. **c**, Nucleation of skyrmions and stripes with unipolar pulse trains. The injection of millions of pulses (each 180 ns in width) leads to the formation of stripe domains at low current densities. The stripes are aligned parallel to the injected current. At large current densities, skyrmions prevail. The black-and-white contrast denotes magnetization pointing in the +*z* and −*z* directions, respectively. The out-of-plane field in all of the experimental images is $\mu_0 H_z = -3.2$ mT, that is, opposing the newly nucleated domains and skyrmions.

same effect is observed for larger currents, at least up to 6×10^{11} A m^{-2}. Already at slightly lower amplitudes of 2.2×10^{11} A m^{-2}, however, the probability of observing a skyrmion reduces to approximately one-third. The functional dependence $j_c(\tau)$, depicted in Fig. 3g, is qualitatively consistent with the established model for spin–orbit torque switching[12]: At small τ, j_c drops rapidly because a minimum time-integrated injected angular momentum is required for switching. This effect saturates because of the Gilbert damping and the current density required for static switching (Supplementary Information). At longer pulses, thermal effects help to overcome the energy barrier and $j_c(\tau)$ follows an Arrhenius law. Quantitatively, the expected $1/\tau$ and $1/\log(\tau)$ functions[12] are not able to describe our data. We suggest the reason for this deviation is that the temperature is not constant because of Joule heating. We confirm this experimentally by using composite pulses that consist of a short pulse on top of a long low-amplitude pulse. The pulses start with a relative delay of Δt. Switching happens within the fixed timescale of the short pulse. Assuming a constant temperature, we therefore expect that j_c does not depend on Δt. In contrast, we observe that j_c is significantly reduced towards the end of the long pulse (inset of Fig. 3g). This effect can be explained by thermally assisted switching and a still-increasing temperature 70 ns after the start of the long pulse. The finite temperature effects (possibly as well as a lower damping than assumed in the simulations) also explain why our experimentally determined current densities are much lower than in the zero-temperature simulations.

Skyrmions can be shifted along the wire by applying unipolar subthreshold current pulses (pulses that move skyrmions but do not create new ones), as in Supplementary Movie 1. Skyrmions move from pinning site to pinning site, as evidenced by the similar skyrmion positions observed in various images. Skyrmions move in the direction of the current (against the electron flow), which finally confirms their left-handed chirality, the consequently defect-free domain walls and thus the single spherical topology (topological charge $N = 1$)[7]. The maximum displacement with ten pulses of 6 ns length is 500 nm, which corresponds to a velocity of 8 m s^{-1}, in agreement with previous observations[6]. The skyrmion trajectories show no skyrmion Hall effect, which is expected given that the current density of $j = 2.2 \times 10^{11}$ A m^{-2} is only slightly larger than the minimum amplitude to induce motion in this material[8]. After 230 pulses, all the skyrmions have disappeared from the FOV and none appear after more pulses because the skyrmions were generated only within the wire and the wire has a finite length.

The spatial probability distribution of finding negative m_z (skyrmions or domains) after the application of a single pulse is depicted in Fig. 3h. The discrete hot spots in this distribution confirm localized defects to be the origin of skyrmion nucleation. Skyrmions are mostly found within the wire, detached from the edge, which is important for applications. Short pulses predominantly create round skyrmions and—rarely—domains attached to the wire edges. At long pulses, in contrast, we frequently encounter stripe domains oriented parallel to the current, as also observed in Fig. 2a. Short and strong pulses are hence preferable for skyrmion nucleation and for skyrmion motion, which is also helpful for high-speed operations.

Our results so far demonstrate reproducible skyrmion generation and explain the underlying mechanism. However, the location of the

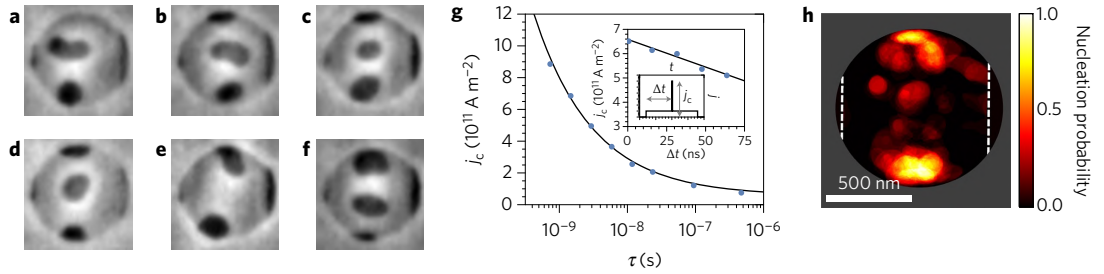

Figure 3 | Creation of skyrmions at natural defects. a–f, Examples of skyrmions nucleated with single 12 ns long pulses of 2.6×10^{11} A m^{-2} amplitude. Before each image, a large magnetic field was temporarily applied to saturate the sample. Skyrmions are often slightly elongated in the y direction. The black contrast at the right side of the images is the edge of the wire and of non-magnetic origin. **g**, Critical current density j_c to nucleate domains with a single pulse as a function of pulse width τ. Inset: critical current density j_c for reproducible domain nucleation with the composite pulse that is schematically shown in the inset of the inset: a 96 ns long base pulse of 0.95×10^{11} A m^{-2} superimposed by a 1.5 ns peak pulse of variable amplitude. The peak pulse j_c is plotted as a function of the delay Δt of the peak pulse with respect to the start of the base pulse. The base pulse amplitude is 25% below the threshold for skyrmion nucleation, and hence serves here primarily as a Joule heater: The longer the delay of the peak pulse, the warmer is the wire and the critical current density decreases. The lines are guides to the eye. **h**, Spatial probability distribution of finding a reversed magnetization after the application of single pulses in the experimental data. Areas of high nucleation probability correspond to strong pinning centres according to the simulation results. The white dashed lines mark the edges of the track. White contrast denotes magnetization pointing down (into the paper plane) and black contrast symbolizes upwards-pointing magnetization. The out-of-plane field for all the images in this figure is $\mu_0 H_z = -6.1$ mT, where the negative sign of the field indicates that it is applied in the direction of the white domains.

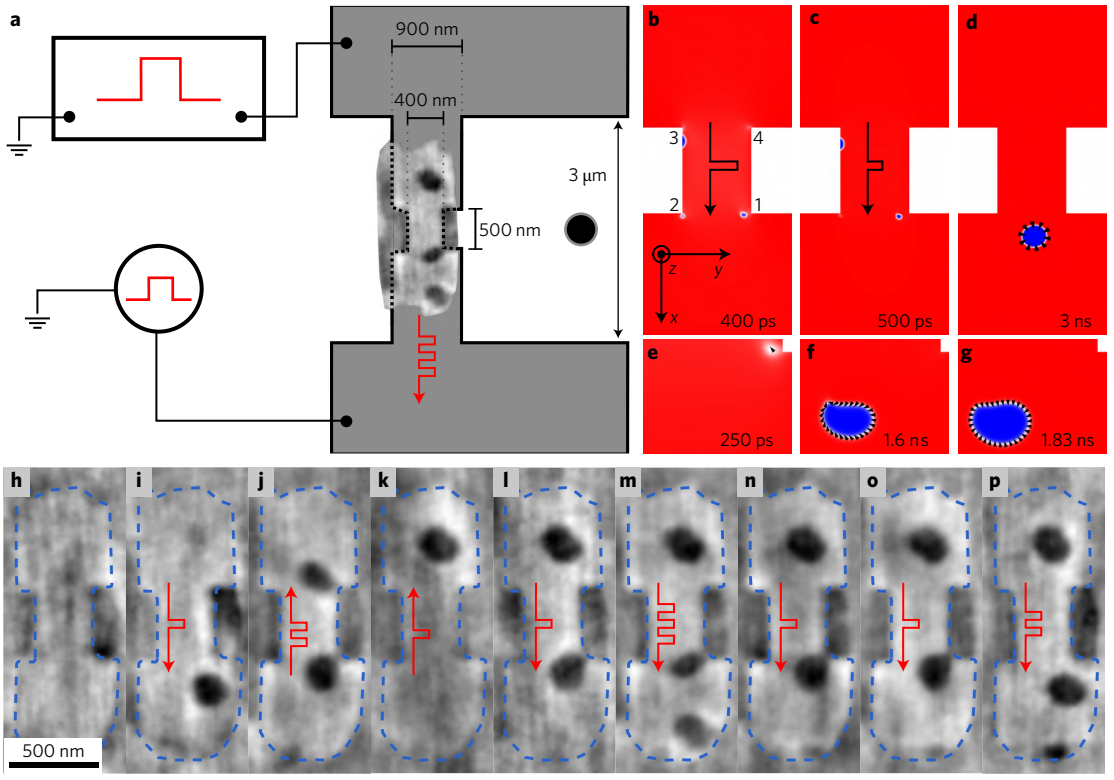

Figure 4 | Demonstration of single-skyrmion generation and subsequent motion. a, Schematic view of the new sample design. With respect to Fig. 2a, a constriction has been added to the wire and the FOV has been enlarged. **b–g**, Micromagnetic simulations of the nucleation process at the constriction, using again a nucleation pulse ($j = 7.0 \times 10^{12}$ A m^{-2}, $\tau = 0.4$ ns) followed by a shift pulse ($j = 3.5 \times 10^{12}$ A m^{-2}, $\tau = 1.2$ ns). Current densities refer to the centre of the constriction. The time that corresponds to each image is given at the bottom right. The corners are numbered in **b**. **e–g**, Magnification of corner 1. **h–p**, Experimental confirmation of the controlled skyrmion nucleation near a constriction. The blue dotted line is the border of the constricted wire within the FOV. The red arrows indicate the direction and number of single $j = 5.8 \times 10^{11}$ A m^{-2}, $\tau = 6$ ns pulses applied prior to imaging the respective frame. The experimental images were obtained in an out-of-plane field of $\mu_0 H_z = -7.1$ mT, where the negative field is applied in the direction of the white domains, that is, into the paper plane.

nucleated skyrmions was not fully predictable, as required for applications, because here we rely on naturally occurring defects. To generate skyrmions deterministically at a predetermined location, we follow the idea of Iwasaki *et al.*[24] and use a tailored defect—namely, a constriction—instead of naturally present pinning sites. We cut the constriction from an existing wire using focused ion-beam milling and also enlarge the FOV, as depicted in Fig. 4a. Simulations suggest that domains nucleate at three out of four corners of the constriction, but only one of those domains is stable after switching off the pulse (Fig. 4b–g). The difference between

corner 1 and corner 2 is mainly that the skyrmion in corner 1 detaches more easily from the edge because of the skyrmion Hall effect. Once it is sufficiently far away from the edges, it becomes more stable, which explains why this domain survives and the other two annihilate. However, a different shape of the corners can lead to nucleation of a stable domain at corner 2 instead of corner 1. Importantly, though, domains leave the constriction exclusively in the direction of the applied current, independent of pulse shape and details of the geometry. The nucleation mechanism is the same as at bulk pinning sites (see Fig. 4e–g). The gradient of m_z comes from the increased current density at the corners and tilting of spins at the boundaries because of the DMI[24,30].

The experiments confirm the predictions of the micromagnetic simulations (Fig. 4h–p). We started with a saturated wire (Fig. 4h). Subsequently, we recorded a sequence of images at a constant external field of $\mu_0 H_z = -7.1$ mT, that is, without saturating in between. Before each image was acquired, we injected unipolar spin–orbit torque current pulses with a magnitude below the nucleation threshold for the wide part of the wire. We observed reproducible nucleation of single skyrmions selectively at one of the exits of the constriction, determined by the direction of the applied current. Following their nucleation, skyrmions can be moved within the wide part of the wire by applying more current pulses. New skyrmions are generated once the existing skyrmion has moved away and sufficient space is available. The constriction itself is too narrow for skyrmions to survive. Hence, skyrmions are repelled from the entrance of the constriction and annihilate when they are forced to enter nonetheless (Fig. 4j,k). Our sample shows significant natural pinning, as revealed by the resistance to motion of the nucleated skyrmions. However, this can be amended by further material- and fabrication-process optimization[7].

Our results demonstrate that skyrmion generators can be integrated into racetrack devices in the simplest way: by patterning of notches or constrictions. We thereby confirm earlier theoretical concepts[24] and extend them to spin–orbit torque devices and materials with interfacial DMI. These simple generators provide full control over where and when skyrmions are nucleated at timescales and voltages that match present-day computer architectures. Constriction-type skyrmion generators can become transparent by making them wide enough to fit a skyrmion comfortably, which is important if such elements are to be used in positions other than the ends of a racetrack memory. All ambiguity as to the exact point of nucleation can be removed by using triangular-shaped notches with only one corner. Hence, the final remaining fundamental challenge for a prototype skyrmion racetrack memory is the controlled annihilation of a skyrmion.

Methods

Methods and any associated references are available in the online version of the paper.

References

1. Nagaosa, N. & Tokura, Y. Topological properties and dynamics of magnetic skyrmions. *Nat. Nanotech.* **8,** 899–911 (2013).
2. Büttner, F. *et al.* Dynamics and inertia of skyrmionic spin structures. *Nat. Phys.* **11,** 225–228 (2015).
3. Yu, X., Tokunaga, Y., Taguchi, Y. & Tokura, Y. Variation of topology in magnetic bubbles in a colossal magnetoresistive manganite. *Adv. Mater.* **29,** 1603958 (2016).
4. Jiang, W. *et al.* Blowing magnetic skyrmion bubbles. *Science* **349,** 283–286 (2015).
5. Moreau-Luchaire, C. *et al.* Additive interfacial chiral interaction in multilayers for stabilization of small individual skyrmions at room temperature. *Nat. Nanotech.* **11,** 444–448 (2016).
6. Woo, S. *et al.* Observation of room-temperature magnetic skyrmions and their current-driven dynamics in ultrathin metallic ferromagnets. *Nat. Mater.* **15,** 501–506 (2016).
7. Litzius, K. *et al.* Skyrmion Hall effect revealed by direct time-resolved X-ray microscopy. *Nat. Phys.* **13,** 170–175 (2017).
8. Jiang, W. *et al.* Direct observation of the skyrmion Hall effect. *Nat. Phys.* **13,** 162–169 (2016).
9. Sinova, J., Valenzuela, S. O., Wunderlich, J., Back, C. H. & Jungwirth, T. Spin Hall effects. *Rev. Mod. Phys.* **87,** 1213–1260 (2015).
10. Brataas, A. & Hals, K. M. D. Spin–orbit torques in action. *Nat. Nanotech.* **9,** 86–88 (2014).
11. Liu, L. *et al.* Spin-torque switching with the giant spin Hall effect of tantalum. *Science* **336,** 555–558 (2012).
12. Garello, K. *et al.* Ultrafast magnetization switching by spin–orbit torques. *Appl. Phys. Lett.* **105,** 212402 (2014).
13. Lee, K.-S., Lee, S.-W., Min, B-C. & Lee, K.-J. Threshold current for switching of a perpendicular magnetic layer induced by spin hall effect. *Appl. Phys. Lett.* **102,** 112410 (2013).
14. Huang, K.-F., Wang, D.-S., Tsai, M.-H., Lin, H.-H. & Lai, C.-H. Initialization-free multilevel states driven by spin–orbit torque switching. *Adv. Mater.* **29,** 1601575 (2017).
15. Legrand, W. *et al.* Room-temperature current-induced generation and motion of sub-100 nm skyrmions. *Nano Lett.* **17,** 2703–2712 (2017).
16. Parkin, S. S. P., Hayashi, M. & Thomas, L. Magnetic domain-wall racetrack memory. *Science* **320,** 190–194 (2008).
17. Fert, A., Cros, V. & Sampaio, J. Skyrmions on the track. *Nat. Nanotech.* **8,** 152–156 (2013).
18. Wiesendanger, R. Nanoscale magnetic skyrmions in metallic films and multilayers: a new twist for spintronics. *Nat. Rev. Mater.* **16044** (2016).
19. Rosch, A. Skyrmions: moving with the current. *Nat. Nanotech.* **8,** 160–161 (2013).
20. Hellman, F. *et al.* Interface-induced phenomena in magnetism. *Rev. Mod. Phys.* **89,** 025006 (2017).
21. Sampaio, J., Cros, V., Rohart, S., Thiaville, A. & Fert, A. Nucleation, stability and current-induced motion of isolated magnetic skyrmions in nanostructures. *Nat. Nanotech.* **8,** 839–844 (2013).
22. Romming, N. *et al.* Writing and deleting single magnetic skyrmions. *Science* **341,** 636–639 (2013).
23. Koshibae, W. *et al.* Memory functions of magnetic skyrmions. *Jpn J. Appl. Phys.* **54,** 053001 (2015).
24. Iwasaki, J., Mochizuki, M. & Nagaosa, N. Current-induced skyrmion dynamics in constricted geometries. *Nat. Nanotech.* **8,** 742–747 (2013).
25. Zhou, Y. & Ezawa, M. A reversible conversion between a skyrmion and a domain–wall pair in a junction geometry. *Nat. Commun.* **5,** 4652 (2014).
26. Hrabec, A. *et al.* Current-induced skyrmion generation and dynamics in symmetric bilayers. *Nat. Commun.* **8,** 15765 (2017).
27. Schott, M. *et al.* The skyrmion switch: turning magnetic skyrmion bubbles on and off with an electric field. *Nano Lett.* **17,** 3006–3012(2017).
28. Eisebitt, S. *et al.* Lensless imaging of magnetic nanostructures by X-ray spectro-holography. *Nature* **432,** 885–888 (2004).
29. Büttner, F. In *Holographic Materials and Optical Systems* (eds Naydenova, I., Babeva, T. & Nazarova, D.) Ch. 10 (InTech, 2017).
30. Rohart, S. & Thiaville, A. Skyrmion confinement in ultrathin film nanostructures in the presence of Dzyaloshinskii–Moriya interaction. *Phys. Rev. B* **88,** 184422 (2013).

Acknowledgements

This work was supported by the US Department of Energy, Office of Science, Basic Energy Sciences under Award no. DE-SC0012371. F.B. acknowledges financial support by the German Science Foundation under grant no. BU 3297/1-1.

Author contributions

F.B., B.P., S.E. and G.S.D.B. conceived and designed the experiment. F.B., I.L., M.S., C.M.G. and D.E. prepared and pre-characterized the samples. F.B., I.L., M.S., B.P., P.H., J.G. and L.C. performed the experiments with support by J.V. B.P. and P.H. reconstructed the holographic images. I.L., F.B. and B.K. performed the micromagnetic simulations. F.B. drafted the manuscript. S.E. and G.S.D.B. supervised the project. All the authors discussed the results, the implications and the figures, and commented on the manuscript.

Additional information

Supplementary information is available in the online version of the paper. Reprints and permissions information is available online at www.nature.com/reprints. Publisher's note: Springer Nature remains neutral with regard to jurisdictional claims in published maps and institutional affiliations. Correspondence and requests for materials should be addressed to F.B.

Competing financial interests

The authors declare no competing financial interests.

Methods

Simulation details. In the simulation images, blue indicates positive m_z and red indicates negative m_z. Simulations were performed at zero temperature using the MuMax software[31], employing the effective medium model[6] to simulate the experimental magnetic multilayer as one isotropic medium with one cell in the z direction. Material parameters were chosen to mimic the materials in the experiments (Supplementary Information). Specifically, the single layer saturation magnetization $M_s = 1.12 \times 10^6$ A m^{-1} and anisotropy constant $K_u = 9.78 \times 10^5$ J m^{-3} were determined experimentally by vibrating sample magnetometry. Exchange and DMI constants $A = 10^{-11}$ J m^{-1} and $D_i = 1.5 \times 10^{-3}$ J m^{-2} were chosen in agreement with the observed stripe domain width of the demagnetized state of 150–200 nm, as measured by magnetic force microscopy (and confirmed in Fig. 2c). Simulation cells with a lateral edge length of 2.25 nm were used. Out-of-plane magnetic fields of $\mu_0 H_z = -57.5$ mT and −50 mT are applied in Figs 1 and 4, respectively. Spin–orbit torque effects were simulated using the available solver for Slonczewski spin valves. To convert the parameters of this solver into transverse spin Hall currents, a spin Hall angle of $\theta_{SH} = 0.07$ was assumed. The coefficient of the field-like torque H_{FL} was adjusted to half of the coefficient of the damping-like torque H_{DL}. The current distribution for the constricted wire (Fig. 4b–g) was determined using a finite-differences solver with a given constant voltage at the sample edges.

Experimental details. The magnetic multilayers were grown on a Si_3N_4 membrane with a seed layer of Ta(2.3 nm)/Pt(3.7 nm) by d.c. (Ta, Pt and $Co_{60}Fe_{20}B_{20}$) and radiofrequency (MgO) sputtering using Ar plasma at a pressure between 3 mTorr (Ta, $Co_{60}Fe_{20}B_{20}$ and MgO) and 3.5 mTorr (Pt). The thicknesses were estimated from sputtering times and calibrated sputtering rates. The thickness of the MgO layers is approximate because we observed fluctuations in the respective rate. Hysteresis loops of the material are provided in the Supplementary Information. The magnetic material was patterned into 10 μm wide tracks by shadow-mask lithography (using a membrane frame without the membrane) and further narrowed using a focused ion beam (with a 30 keV Ga^+ ion beam of an FEI Helios 600 Nanolab dual-beam instrument). The Si_3N_4 membrane substrates were equipped with a holographic mask on the back side (see Büttner[29] for further details). Imaging was performed at beamline P04 at PETRA III, DESY, using X-ray holography with circular polarized X-rays of 778 eV photon energy[29]. The reference holes had a diameter of 25 nm, 120 nm and 110 nm in Figs 2–4, respectively. Samples were investigated in vacuum at room temperature. Purely out-of-plane oriented fields of $\mu_0 H_z = -3.2$ mT, −6.1 mT and −7.1 mT were applied during the imaging of the magnetization in Figs 2–4, respectively, in which these fields were accurately calibrated after the measurements using a Hall probe at the same position of the sample and driving the same field cycle as in the experiments. In all experimental magnetization images, black indicates positive m_z and white indicates negative m_z, where the coordinate system is defined in Fig. 1.

Data availability. The data that support the plots within this paper and other findings of this study are available from the corresponding author on reasonable request.

References

31. Vansteenkiste, A. *et al.* The design and verification of MuMax3. *AIP Adv.* **4**, 107133 (2014).